



Near-Surface Carbon-Dioxide Tunable Diode Laser Absorption Spectroscopy Concentration Measurements in Hypervelocity Flow

Joshua M. Weisberger* and Paul E. DesJardin†

University at Buffalo, State University of New York, Buffalo, New York 14260

and

Matthew MacLean,‡ Ronald Parker,‡ and Zakery Carr§

Calspan — University at Buffalo Research Center, Buffalo, New York 14225

DOI: 10.2514/1.A33251

Measurements of carbon-dioxide concentration are made in the LENS-XX expansion tunnel at the Calspan — University at Buffalo Research Center to investigate the effects of surface catalysis in hypersonic flows. A tunable diode laser absorption spectroscopy setup probes the P36e CO₂ absorption line of the $\nu_1 + \nu_3$ combination band at 2.7153 μm . Numerical simulations are computed with data-parallel line relaxation using the specified reaction efficiency surface catalysis model. Absorption measurements adjacent to the surface of an aluminum cylinder correlate well with simulations indicating low catalytic efficiency at the surface. The velocity, density, freestream temperature, specific enthalpy, and stagnation point pitot pressure of the run are 4.6 km/s, 1.53 g/m³, 1328.4 K, 11.75 MJ/kg, and 31.6 kPa, respectively. Simulation of the absorption spectrum is performed using a nonhomogeneous line-by-line code using the high-resolution transmission molecular absorption database for spectroscopic parameters. Input data for the code are obtained from computational fluid dynamics simulations of the cylinder and facility. The specified reaction efficiency for the mechanism $\text{CO} + \text{O} \rightarrow \text{CO}_2$ is determined inversely using detailed computational fluid dynamics and comparisons to experimental measurements. The best agreement was found for $\gamma_{\text{CO}} = 0.00025$ to 0.0005, indicating that the coupled line-by-line code and computational fluid dynamics approach is useful for assessing near-surface composition using tunable diode laser absorption measurements of hypersonic flows.

Nomenclature

a_n	=	coefficients for polynomial, Lorentzian, and Gaussian baseline functions
E''	=	transition lower-state energy, cm ⁻¹
hc/k	=	second radiation constant, cm · K
I	=	transmitted intensity
I_o	=	incident intensity
k_ν	=	spectral absorption coefficient, cm ⁻¹
$k_\nu L$	=	absorbance
L	=	optical path length, cm
M	=	molecular weight of absorbing molecule, g · mol ⁻¹
n	=	collisional broadening exponent
P_j	=	total pressure of j th zone, atm
Q	=	partition function
S	=	temperature-dependent transition linestrength, cm ⁻² · atm ⁻¹
$S_{i,j}$	=	linestrength of i th transition and j th zone, cm ⁻² · atm ⁻¹
T	=	temperature, K
T_j	=	temperature of j th zone, K
\dot{w}	=	molar production rate, mol · m ⁻² · s ⁻¹
X_j	=	absorbing species mole fraction of j th zone
x_i	=	line-center index
Y	=	absorbing species mass fraction
Γ	=	CO impingement flux, mol · m ⁻² · s ⁻¹
γ	=	catalytic recombination parameter

$\Delta\nu_C$	=	collisional broadening full width at half-maximum, cm ⁻¹
$\Delta\nu_D$	=	Doppler broadening full width at half-maximum, cm ⁻¹
Δx	=	zone path length, cm
δ_{air}	=	air-broadening half-width, cm ⁻¹ · atm ⁻¹
δ_{self}	=	self-broadening half-width, cm ⁻¹ · atm ⁻¹
ν_i	=	wavenumber of i th transition, cm ⁻¹
ν_o	=	line-center wavenumber, cm ⁻¹
φ	=	transition lineshape function, cm
$\varphi_{i,j}$	=	lineshape function for i th transition and j th zone, cm

I. Introduction

MARS has become the primary focus for planetary exploration missions. When entering its atmosphere at hypersonic speeds, a shock wave develops in front of the vehicle. The kinetic energy associated with flight at these speeds results in extremely high temperatures behind the shock. To retain the structural integrity of the vehicle, a thermal protection system (TPS) is often used to protect against the harsh environment. High-speed entry is a critical design consideration, and the design of an adequate TPS is crucial for decreasing the weight of the vehicles and cost of the launches. Aerothermal heating includes contributions from radiation, convection, and air/surface chemistry. An important source of chemical heating is the catalytic exothermic recombination of atoms and molecules on the TPS surface. Often, the TPS is overdesigned by using the most conservative estimate for heat flux, which corresponds to the supercatalytic boundary condition. Using a more accurate surface catalysis model can allow for more efficient designs of the TPS for a given vehicle and mission.

The Martian atmosphere is made up of approximately 95.7% CO₂ with other trace species. Catalytic heating does occur for Earth reentry, but it is more pronounced in the carbon-dioxide environments of Mars. This is in part due to the large exothermic recombination reaction of CO and O forming CO₂ [1]. Recombination at or near the surface of species dissociated in the shock layer leads to higher levels of heating at the vehicle surface due to the energy released from the recombination process. At higher speeds, the effects of catalysis become increasingly important when calculating heat loads on the

Received 15 January 2015; revision received 31 May 2015; accepted for publication 14 June 2015; published online 9 September 2015. Copyright © 2015 by the American Institute of Aeronautics and Astronautics, Inc. All rights reserved. Copies of this paper may be made for personal or internal use, on condition that the copier pay the \$10.00 per-copy fee to the Copyright Clearance Center, Inc., 222 Rosewood Drive, Danvers, MA 01923; include the code 1533-6794/15 and \$10.00 in correspondence with the CCC.

*Graduate Student, Mechanical and Aerospace Engineering. Student Member AIAA.

†Professor, Mechanical and Aerospace Engineering. Senior Member AIAA.

‡Senior Research Scientist. Senior Member AIAA.

§Research Scientist. Member AIAA.

surface [2]. Uncertainty in catalytic behavior of the surface is a challenge when trying to find heating rates and transition onset criteria [3]. The main problem that catalysis poses is that, in order to understand ground test measurements and validate computational fluid dynamics (CFD) using those measurements, the surface catalysis of the particular model tested must be known and an extrapolation is necessary to both the environment and the TPS material of the flight vehicle. However, catalytic mechanisms are not fully understood.

Certain mechanisms have been postulated to be present, including the Langmuir–Hinshelwood (L-H) and Eley–Rideal (E-R) mechanisms. The L-H mechanism describes the interaction between two adsorbed molecules, whereas the E-R mechanisms describe the interaction between an adsorbed molecule and a gas phase molecule. Catalytic surface modeling has been taken into account in recent CFD codes [4,5]. There are multiple methods of including catalytic wall boundary conditions, with some more physical than others. The noncatalytic and supercatalytic surface boundary conditions provide lower and upper bounds on surface heating, respectively. In the supercatalytic case, the gas mixture is returned to its lowest chemical energy state at the wall, releasing the energy back into other modes in the flow. For cold-wall ground test environments in a pure CO_2 test gas, this corresponds to the CO_2 returning back to its freestream mass fraction of unity. This boundary condition is nonphysical because it does not include rate limitation or reactant availability in describing how the recombination has occurred. A specified reaction efficiency (SRE) model has been used in which a catalytic recombination efficiency is specified that relates the number of reactants that recombine at the surface to the total number that reach the surface. The SRE model is more physical, in that it accounts for reactant and product availability through species mass balance at the surface, but the reaction efficiency γ must be known for each reaction, and specifying significant numbers of reactions in which reactants are consumed by multiple pathways can be very complex. Quantification of individual reaction pathways that provide the most significant energetic changes to gas composition is therefore critical in implementing a relevant surface catalysis model.

Clearly, state-of-the-art hypersonic flow modeling suffers from unknown properties near the vehicle surface. The objective of this study is to provide some of this missing information using tunable diode laser absorption spectroscopy (TDLAS) measurements. TDLAS has been around since the early 1980s, and measurement capabilities continue to improve rapidly with advancing technology in the fields of diode lasers, optics, and detectors. Recent reviews on the use of TDLAS can be found in [6] for application to low-speed reacting flows. Significant additional challenges are also introduced with the application of TDLAS to high-speed flows. Due to the very short test times, the laser must tune extremely fast. Obtaining good signal to noise is challenging because it is not possible to obtain multiple absorption sweeps that can be used for averaging. TDLAS experiments have been successfully performed in NO [7–11], H_2O [12–14], CO [13,15], and CO_2 [16–19] environments. A TDLAS system used for monitoring CO_2 at $2.7\ \mu\text{m}$ was successfully constructed and tested in both a free piston tunnel (VKI Longshot) and an arc jet tunnel (ONERA F4) [20]. This study represents the first use of TDLAS measuring CO_2 at a wavelength of $2.7153\ \mu\text{m}$ ($3682.765\ \text{cm}^{-1}$) in a high-speed expansion tunnel where CO_2 absorption measurements are made in the near-field flow of an aluminum cylinder. These measurements are compared to numerical modeling predictions using line-by-line (LBL) calculations coupled with CFD predictions.

The rest of this study is organized as follows. Section II describes the experimental setup using the Calspan — University at Buffalo Research Center (CUBRC) Large Energy National Shock (LENS)-XX tunnel facility and TDLAS measurements. Section III details the LBL and CFD modeling employed for comparison to measurements. Sections IV and V summarize the processing of the raw TDLAS data and present the results showing comparisons of model predictions to data. Finally, Sec. VI concludes the paper.

II. Experiments

A. LENS-XX Facility and Experimental Setup

CUBRC currently operates a 48 in. shock tunnel, the LENS-I and LENS-II reflected shock tunnels, and the LENS-XX expansion tunnel. These tunnels are used for aerothermal and aero-optic testing and evaluation of flight vehicles. In this study, measurements are conducted in LENS-XX. The appeal of using this facility is that the maximum temperature of the gas before interaction with the test article is significantly lower than from a reflected shock tube or arc jet facility, thereby more closely matching reentry flight conditions and minimizing freestream contamination from gas dissociation.

Peak temperatures in the reflected shock tunnels are extremely high because the energy is added through a strong shock that stagnates the test gas. This leads to dissociation of the test gas that affects the chemical composition of the freestream flow. In an expansion tunnel, the majority of the energy is added to the flow through an unsteady expansion process. This results in a test gas that is free of dissociated species. Measurements can then be made in conditions that more accurately mimic the flight of hypervelocity vehicles, and it is especially important when characterizing surface catalysis. Further details of the facility can be found in work by Dufrene et al. [21,22]

In this study, the experiment consists of a cylindrical model composed of aluminum 2 in. (5.08 cm) in diameter and 2.5 in. (6.35 cm) in span, supported in the facility by rods from the aft (back) side of the cylinder, as seen in Fig. 1. The cylinder is turned on a lathe before installation in the facility to ensure a smooth surface. The cylinder is exposed to air before the test, and the usual oxide layer forms on the surface. The test section width is 2 ft, and it is located in the expansion tube section of the facility. This allows for simpler interpretation of the results because the free jet shear layer that accompanies expansion into the 8 ft test section need not be included. The test condition in the facility is monitored by a pitot probe mounted a few inches above the cylinder and placed in line with the front edge of the cylinder surface, which signals the arrival of the test gas and the duration of steady flow, which lasts about $400\ \mu\text{s}$ for this particular condition. A plot of the time-varying pitot pressure can be seen in Fig. 2. The test gas for this flow condition is composed of a partial pressure of 25% CO_2 and 75% air. This composition is selected for two reasons. The first is to maximize sensitivity of the absorption feature without fear of oversaturation. Data presented in the literature support both the fully catalytic and near-noncatalytic nature of the wall. Using preliminary CFD simulations with predicted characteristic parameters of the flow, a typical laser line-of-sight (LOS) simulation was used to anticipate the absorption spectrum for the two catalytic extremes. The selected absorption line and freestream



Fig. 1 Aluminum cylinder installed in LENS-XX expansion tunnel.

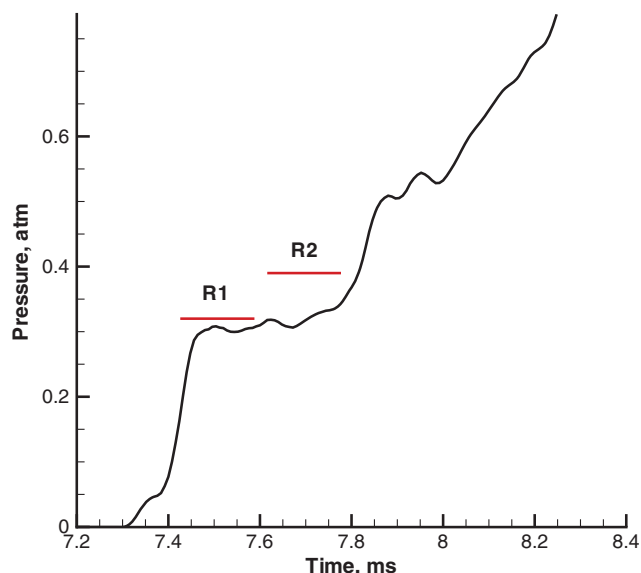


Fig. 2 Time-varying pitot pressure during the entire run. Ramp 1 and ramp 2 time durations are shown as red lines.

composition allowed for adequate absorption, should the flow be noncatalytic, while remaining well below the saturation level, should the flow be fully catalytic. The second is to produce a test condition with an elemental composition similar to that produced by equilibrium ablation of a carbon ablator. The short-term goal of the experiment is to obtain cold-wall catalytic production data for CO_2 , whereas the long-term goal of the effort is to employ the diagnostic and reduction technique for hot-wall (flight-relevant) production of carbon species by catalytic and oxidation processes.

The freestream condition for this run is as follows: $P = 516$ Pa, $T = 1328.4$ K, $\rho = 0.00153$ kg/m³, $U = 4603$ m/s ($M = 7.1$), $Y_{\text{CO}_2} = 0.337$, $Y_{\text{N}_2} = 0.507$, and $Y_{\text{O}_2} = 0.156$. The freestream enthalpy is 11.75 MJ/Kg. All thermal degrees of freedom can be considered in equilibrium with translation. The surface temperature of the cylinder remains fixed at its initial value of 300 K due to the short run time. The pitot pressure at the stagnation point of the cylinder is 31.6 kPa. For this test case, the presence of CO_2 in the freestream complicates the line-of-sight integration of the absorption measurement, but because the pressure is significantly lower, the shape of the absorption signal is very different than that obtained for the surface. Therefore, it is straightforward to differentiate the two effects.

B. Line Selection for TDLAS

The selection of a molecular transition to probe depends on factors such as cost of the laser, availability of materials, interference of other spectral lines, sufficient absorption through the anticipated medium without saturation, scan range of the laser, and sensitivity to appropriate flow parameters. A set of guidelines for selecting an absorption transition has been published by Zhou et al. [23]. The pressure in the shock layer stays nearly constant at approximately 0.3 atm, so only the sensitivities to changes in temperature and concentration are computed. The sensitivity is defined as the change in half-width of the feature per change in temperature or mole fraction. The particular CO_2 line in this study is selected because a conveniently packaged laser was available, other transitions do not interfere with the measurement, and sensitivities to temperature and concentration are high at the expected test conditions. The final selection is a laser that is capable of scanning the wavenumber region between approximately 3682.5 and 3683 cm^{-1} .

It is necessary to ensure the absorption lines from the water vapor in the laboratory air do not interfere with the measurement because the laser will pass through air on either side of the facility windows. The simulated spectra of both CO_2 and H_2O in the wavenumber scan range of the laser can be seen in Fig. 3. The parameters used for the

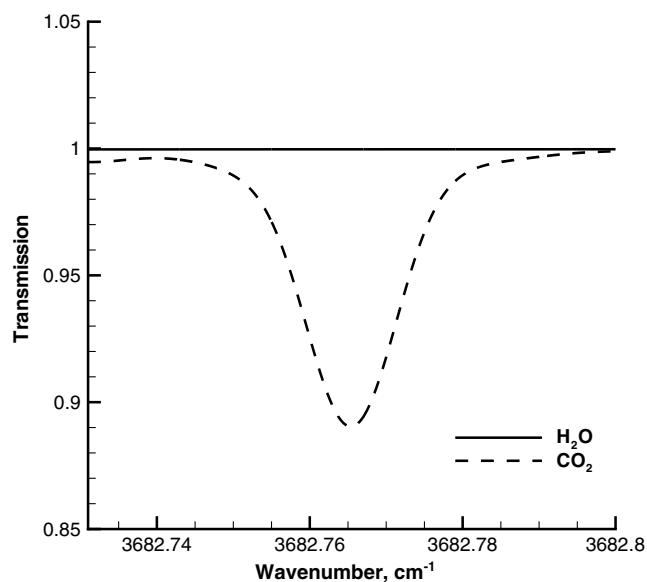


Fig. 3 Transmission plot from simulation of normal run CO_2 levels and nominal laboratory conditions for H_2O experienced during a run.

H_2O simulation are based on normal conditions in the laboratory, and they take into account the distance the laser travels through the air in the experimental setup; the path length is 60 cm, the temperature is 300 K, the pressure is 1 atm, and the mole fraction is 0.01. The contribution from the water in the laboratory atmosphere over the measured path length is nearly undetectable, indicating that this CO_2 line is a reasonable choice for these specific measurements.

C. Diagnostic Measurement Setup

The TDLAS setup operates as a pitch/catch system that spans the LENS-XX test section perpendicular to the flow direction. A schematic of the optical bench setup is shown in Fig. 4. The infrared (IR) laser light source is modulated from the pitch side of the tunnel, whereas the detector and acquisition system are operated from the catch side. The 0.635-cm-diam beam leaving the laser housing is collimated and turned 90 deg through the use of a periscope assembly (Thorlabs, Inc.) to pass through the tunnel. The periscope allows lateral and multiple angular degrees of freedom when aligning the laser along the cylinder surface. The laser enters and exits the tunnel through two 1.75-in.-diam (clear aperture) CaF_2 windows with 30 min of wedge to reduce etaloning. CaF_2 windows are used for the tunnel windows due to their high transmission in the IR region, as well as their low index of refraction, which allows them to be used without an antireflective coating. Beam steering from the wedge is taken into account during the alignment process. The size of the smallest aperture in the system is large enough to ensure that the measurement is diffraction limited. From the pitch side of the optical setup, the collimated laser source is carefully aligned to follow the

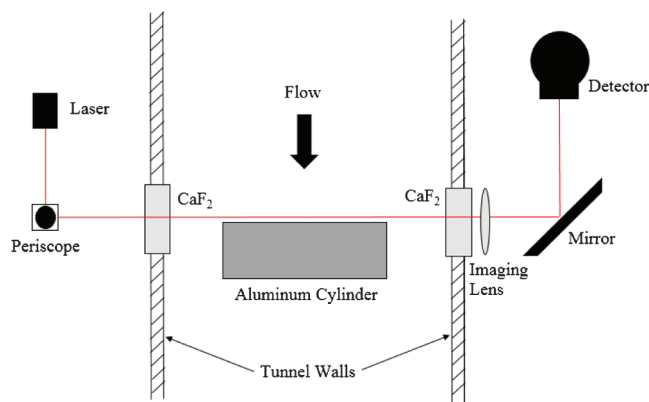


Fig. 4 Top-view schematic of experimental optical bench setup.

cylinder surface as it traverses the tunnel. In this arrangement, a ray from the laser source samples gas at a distance from the surface that remains constant over the cylinder length. After exiting the tunnel and passing through an achromatic imaging lens optimized for mid-IR wavelengths, the beam is split in two. Half the light is sent to the detector, whereas the other half is imaged onto a 640×512 pixel array IR camera to provide real-time images to check the alignment and verify the magnification.

The distributed feedback quantum cascade laser (NanoPlus, GmbH) used in the experiment provides a scanning wavenumber range from 3682.5 to 3683.0 cm^{-1} . A narrower tuning range between approximately 3682.71 to 3682.81 cm^{-1} is used during the test to scan more slowly through the feature, avoiding lineshape smearing and increasing the number of data points describing the absorption feature. The beam is rapidly modulated to scan over this range by varying the temperature and injection current. The wavelength can be coarsely tuned by adjusting the temperature via the thermoelectric device to which the diode is mounted. For fine-tuning capabilities, an ILX Lightwave LDC-3724C laser diode controller regulates the temperature and current input to the laser, and it receives as input the triangular sawtooth waveform from a Tektronix AFG3102 arbitrary waveform generator. The LN₂ cooled InSb 32-element linear array infrared detector (L-3 Cincinnati Electronics model SDD-2000-32-H) is coupled to a data-acquisition system to acquire and store the signal at a frequency of 100 MHz.

The laser has an emission linewidth of less than 3 MHz (0.0001 cm^{-1}). At a scanning frequency of up to 6 kHz, this resolution has been shown to have a minimal effect on the measured absorption feature lineshape and can be neglected. At high modulation rates, the ideal linear ramp starts to become nonlinear. Based on experience, the realistic maximum frequency for operation in a linear range is about 5 kHz. At this frequency, there will be four ramps per millisecond. For each ramp, the feature should have a sufficient amount of data points to accurately describe its shape, amplitude, and position. The bandwidth of the data acquisition system dictates how many data points will be acquired in the ramp. With a bandwidth of 100 MHz, 25,000 samples are acquired per ramp. This amount is more than sufficient to accurately capture the lineshape of the absorption feature. The temperature of the temperature controller is set to 25°C, and the modulation of the ramp amplitude is 0.56 V. The current is set to 140 mA, and the frequency of the waveform is 5 kHz.

Although expansion tunnels can cause significant amounts of mechanical vibration, there is no movement of the facility until after the data are collected. This is verified using multiple channels on the linear array detector. When initially setting up the experiment, some of the pixels are shadowed by the cylinder surface. Movement of the shadow of the cylinder in the recorded data of the individual pixel elements occurs only after the test time is over.

III. Modeling and Data Analysis

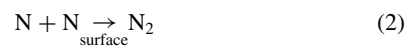
A. Computational Fluid Dynamics

The data-parallel line relaxation (DPLR) code, developed by the NASA Ames Research Center, is the tool used for the CFD portion of the analysis of the experiment. DPLR is a multiblock, structured, finite volume code that solves the reacting Navier–Stokes equations including finite rate chemical and thermal nonequilibrium effects. The code is based on the data-parallel line relaxation method [24] and implements a modified low-dissipation Steger–Warming flux splitting approach [25] for the convection terms and central differencing for the diffusion terms. Transport properties for the reacting mixtures are modeled in DPLR for high-enthalpy flow [26,27] using the binary collision-integral-based mixing rules from Gupta et al. [28] with a database of relevant collision integral data for high-temperature collisions [29,30]. Diffusion coefficients are modeled using self-consistent effective binary diffusion [31]. The DPLR code allows an arbitrary set of chemical species and reactions to be used. In this work, a standard eight-species air/carbon-dioxide species set (CO₂, CO, N₂, O₂, NO, C, N, O) was employed using the set of reaction rates published by Park et al. [32]. Reverse reactions rates were computed from equilibrium. Finite rate vibrational relaxation is

modeled via a simple harmonic oscillator vibrational degree of freedom [33] using the Landau–Teller model [34]. Vibrational energy relaxation rates are computed by default from the semiempirical expression from Millikan and White [35], but rates from the work of Camac [36] and Park et al. [32] are substituted for specific collisions where experimental data exists. Vibration–dissociation coupling is currently modeled using the $T - T_v$ approach of Park [37].

The noncatalytic wall boundary condition enforces zero catalytic production for each species, which implies that diffusion flux for each will be zero. The supercatalytic boundary condition sets a mixture composition explicitly at the surface that coincides with the lowest energy composition of the gas without regard for reaction kinetics or reactant availability. The supercatalytic boundary condition enforces a nonphysical set of catalytic production rates at the surface, but it does provide an upper limit on energy release at the surface, and thus a conservative estimate for design of the TPS. The SRE model enforces a user-specified efficiency for catalytic reactions based on the fraction of reactant species that reach the surface for which a recombination event occurs. The reaction efficiency (or reactant loss efficiency) γ may be specified as constant or as a function of temperature resulting from an empirical curve fit of experimental data. Very recently, a generalized physics-based finite rate surface chemistry (FRSC) model [4,5] has been implemented in the DPLR code that allows for an arbitrary number of physical reaction forms, such as E-R and L-H recombination events to be specified. The FRSC model requires specification of a large number of physical parameters that must be obtained for each environment and has not yet gained widespread use.

For mixed air/carbon-dioxide systems, a number of outcomes affecting the energy balance at the surface are possible, including those listed in Eqs. (1–4):



Besides homogeneous atom recombinations, given in Eq. (1) and Eq. (2), heterogeneous recombination producing nitric oxide has been recently suggested as an important surface catalytic mechanism for reacting air [10]. For dominantly carbon-dioxide systems, such as would be relevant for Martian entry applications, the competition between Eq. (1) and Eq. (4) for consumption of atomic oxygen results in very different heat flux to the surface [38]. Evidence by Sepka et al. [39] suggested that Eq. (4) should occur with relatively low efficiency for surfaces at or near room temperature because of the large energy barrier of CO [40]. However, little is known about this mechanism at hypersonic flight-relevant conditions, and experiments in shock tunnel environments have shown heat flux results that are consistent with highly efficient CO₂ production at the surface [3,41]. Only the reaction in Eq. (4) is used in this study. The reaction from Eq. (1) is included with Eq. (4) in a single case to investigate the effects of specifying a nonzero O₂ recombination parameter. In this case, the recombination parameters for CO and O are 0.0005 and 0.010, respectively. Because the percent difference in the simulated absorption is less than 1/10th of a percent, the reaction in Eq. (1) is ignored for the rest of the study. In this work, the catalytic recombination efficiency parameter is defined in Eq. (5) as the fraction of CO molecules reaching the surface that participate in a recombination to CO₂ via the reaction pathway in Eq. (4). Its value ranges from zero to unity:

$$\gamma_{\text{cat}} = \frac{-\dot{w}_{\text{CO}}}{\Gamma_{\text{CO}}} = \frac{-\dot{w}_4}{\Gamma_{\text{CO}}} \quad (5)$$

The flux of CO to the surface is obtained via kinetic theory. Each recombination event by Eq. (4) also consumes one oxygen atom, but oxygen atoms are simultaneously consumed by other reaction pathways [e.g., Eqs. (1) and (3)]. Molar consumption of CO and molar production of CO₂, however, are clearly linked in a 1 : 1 ratio by Eq. (4). This surface catalysis model is not limited by the assumption of particular site balance reaction models, such as the L-H or E-R models. However, the drawback is that the value of the recombination efficiency parameter has an unknown dependency on factors such as temperature, densities, and surface conditions.

Because the test gas is a mixture of air and carbon dioxide that will be dissociated in the shock layer, several catalytic outcomes are possible for the near-surface region. Downstream of the bow shock in the stagnation region, the calculation of the equilibrium state of the gas is $T_{\text{eq}} = 4425$ K, $P_{\text{eq}} = 30.3$ kPa, $Y_{\text{N}_2, \text{eq}} = 0.493$, $Y_{\text{O}_2, \text{eq}} = 0.006$, $Y_{\text{NO}, \text{eq}} = 0.020$, $Y_{\text{N}, \text{eq}} = 0.005$, $Y_{\text{O}, \text{eq}} = 0.261$, $Y_{\text{CO}_2, \text{eq}} = 0.001$, and $Y_{\text{CO}, \text{eq}} = 0.214$. Although some boundary layer recombination will certainly occur, the gas approaching the surface will be largely composed of carbon monoxide, atomic oxygen, and molecular nitrogen at these conditions.

Although this experiment does not identify a specific physical mechanism through which a surface reaction occurs, it does provide, to the authors' best knowledge, the first direct measurement of the effectiveness of the major reaction pathway described by Eq. (4) at a flight-relevant freestream velocity. The consumption of atomic oxygen cannot be directly analyzed using the measured data in this case, but the reactant loss efficiency of carbon monoxide can be directly fit from the measured data using the techniques outlined here. This effort, therefore, represents a major advancement over the current nonphysical observations made from high-enthalpy facilities by interpreting indirect measurements such as heat flux, surface temperature, or recession rates that are nonlinear functions of multiple simultaneous processes that cannot be easily decoupled.

B. Line-by-Line Model

The theory behind absorption spectroscopy is based on the Beer-Lambert law, which governs the absorption of monochromatic radiation through a uniform path length of a weakly absorbing medium. A discretized approach is used in this study to model the effects of inhomogeneity along the line-of-sight:

$$\frac{I}{I_0} = \exp(-k_\nu L) \quad (6)$$

$$k_\nu L = \sum_j P_j X_j \left[\sum_i S_{i,j}(\nu_i, T_j) \phi_{i,j}(\nu_i, T_j, P_j) \right] \Delta x_j \quad (7)$$

The summation over j is for all the zones along the line-of-sight, whereas the summation over i is for all wavenumbers in the simulation range. Reference linestrength data at 296 K were obtained from the high-resolution transmission molecular absorption (HITRAN) 2008 database [42]. Linestrengths were scaled to other temperatures with the following relation,

$$S(T) = S(T_0) \frac{Q(T_0)}{Q(T)} \left(\frac{T_0}{T} \right) \exp \left[-\frac{hcE''}{k} \left(\frac{1}{T} - \frac{1}{T_0} \right) \right] \left[1 - \exp \left(\frac{-hc\nu}{kT} \right) \right] \left[1 - \exp \left(\frac{-hc\nu}{kT_0} \right) \right]^{-1} \quad (8)$$

A third order polynomial is used to fit the partition function from the given data in the HITRAN database. The lineshape ϕ is a function of multiple types of broadening mechanisms, with some more

important than others. The two dominating mechanisms in this study are Doppler broadening and collisional broadening, with typical full-width at half-maximum (FWHM) values of approximately 0.012 and 0.046 cm⁻¹, respectively. Doppler broadening is caused by the random thermal motion of the absorbing molecules and follows a Maxwellian velocity distribution, resulting in a Gaussian lineshape:

$$\phi_D(\nu) = \frac{2}{\Delta\nu_D} \left(\frac{\ln(2)}{\pi} \right)^{1/2} \exp \left[-4 \ln(2) \left(\frac{\nu - \nu_0}{\Delta\nu_D} \right)^2 \right] \quad (9)$$

The Doppler FWHM is given next, where the final expression is simplified from the intermediate expression to work in wavenumber units:

$$\Delta\nu_D = \nu_0 \left[\frac{8 kT \ln(2)}{mc^2} \right]^{1/2} = 7.1623 \times 10^{-7} \left[\nu_0 \left(\frac{T}{M} \right)^{1/2} \right] \quad (10)$$

Collisional broadening occurs when molecules collide with each other and is modeled using the Lorentzian function. It is assumed that the collisions are binary and that the transition time is fast compared to the collision duration, and it is given by

$$\phi_C(\nu) = \frac{1}{\pi} \frac{\Delta\nu_C/2}{(\nu - \nu_0)^2 + (\Delta\nu_C/2)^2} \quad (11)$$

The collisional FWHM is given by the expression

$$\Delta\nu_C = 2P \left(\frac{T_0}{T} \right)^n [X\delta_{\text{self}} + (1-X)\delta_{\text{air}}] \quad (12)$$

The self-broadening half-width and air-broadening half-width are obtained from the HITRAN database. Doppler broadening is dominant at lower pressures, whereas at higher pressures, collisional broadening is dominant. The Doppler and collisional FWHM values are comparable, and a Voigt profile is needed that describes the convolution of the two lineshapes. An approximate model of the full frequency-space convolution is used in this study [43].

C. Raw Data Analysis

The raw data obtained from the data acquisition system are processed to obtain a plot of transmission versus wavenumber for comparison to simulations. The raw data are measured in volts on the y axis and time on the x axis. The voltage is arbitrary and depends on the setup parameters for the laser and detector. Two of the sawtooth ramps (1 and 2) are investigated further in this paper. Ramp 1 occurs between 7.426 and 7.588 ms, and ramp 2 occurs between 7.616 and 7.777 ms. The raw data are first trimmed down to a single ramp. The entire dataset is shifted so that all voltages are positive. Data just before and after the ramp when the laser is below threshold are included in order to subtract out the background. A linear fit between the pre- and postramp data are used to subtract out the background. The baseline is the portion of the data when the laser is above threshold but the gas is not absorbing. A least-squares fit for a third-order polynomial is used to initially fit the baseline. A nonlinear Chi-squared minimization is then performed to fit a combination of the baseline and absorption feature. The fitting process is iterated using varying baseline bounds until a minimum Chi squared is converged upon. The polynomial, Lorentzian, and Gaussian functions can be seen in Eqs. (13–15) next, where the values of the coefficients a_n are varied until the best fit is obtained using the preceding method:

$$f_{\text{polynomial}}(a_1, a_2, a_3) = a_1 + a_2x + a_3x^2 + a_4x^3 \quad (13)$$

$$f_{\text{Lorentzian}}(a_4, a_5, a_6) = \frac{(a_4 a_5 / 2\pi)}{(x_i - a_6)^2 + (a_5 / 2)^2} \quad (14)$$

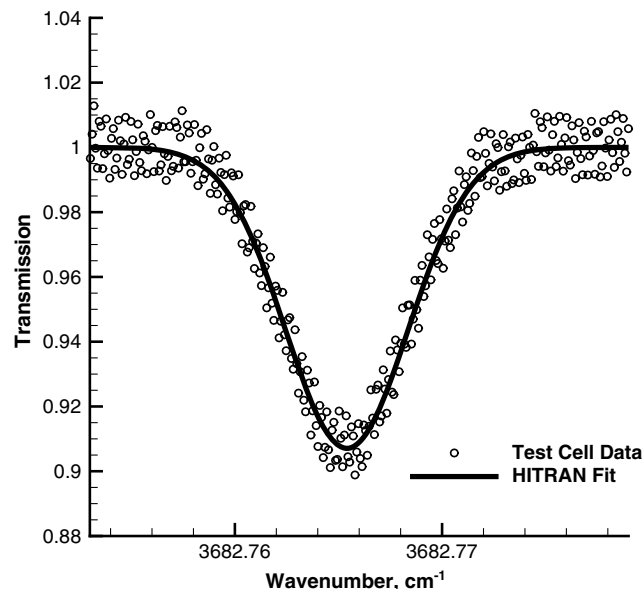


Fig. 5 Example preflow wavenumber calibration showing raw data along with HITRAN simulation fit.

$$f_{\text{Gaussian}}(a_7, a_8, a_9) = \sqrt{\frac{4 \ln 2}{\pi}} \left(\frac{a_7}{a_8} \right) \exp \left[-4 \ln 2 \left(\frac{x_i - a_9}{a_8} \right)^2 \right] \quad (15)$$

The baseline is then divided out, and the raw data transmission spectrum is obtained. The y -axis values are the unitless transmission, whereas the x -axis values are still in an arbitrary index. A wavenumber calibration is needed to transform the x -axis index to wavenumber units.

The wavenumber calibration is obtained using a test cell of known temperature, pressure, path length, and concentration. The test cell used is the actual expansion tube where the main tests are taking place. The section is first pumped down to approximately 25 mTorr. At this level of vacuum, there is still some H_2O in the test section. Pure CO_2 is then injected into the test section until the pressure rises to 55 mTorr, at which point the test cell measurements are taken. A simulation using these parameters is generated, and the slope of the wavenumber calibration (reciprocal centimeters per index) is adjusted until the raw data match the simulation data. The only

unknown in the process is the calibration slope itself. An example of the calibration fit can be seen in Fig. 5. The slope of the wavenumber calibration used in the following data analysis is $-8.479 \times 10^{-5} \text{ cm}^{-1}/\text{index}$. The negative sign is needed because, as the laser current is increased, the wavelength increases. The increase in wavelength corresponds to a decrease in wavenumber. Pretest data were taken over a range of 35 ms to measure the stability of the laser and its wavenumber calibration. The calibration was found to be stable to within 3.4%.

IV. Results and Discussion

A. CFD and Line-by-Line Modeling

An idealized, unsteady, axisymmetric CFD simulation of the entire expansion tunnel is used to obtain the freestream mole fraction, normalized temperature, and normalized pressure profiles across the tunnel radius. Centerline values are predicted for the test time using the CUBRC High-Enthalpy Expansion Tunnel Analysis (CHEETAH) code [21]. The normalized profiles are then redimensionalized using the centerline values so that nonideal effects such as diaphragm breaking are accounted for. This simulation accurately captures the boundary layer along the expansion tunnel wall, which has an impact on the overall simulation absorption profile. A plot of these profiles can be seen in Fig. 6. The temperature and pressure profiles used in the simulations are found by multiplying the normalized profiles by the freestream values given in Sec. II.A.

Property data for the LBL method are extracted from the CFD solutions. The extraction procedure interpolates between cells because the curvilinear cells are not necessarily aligned with the straight laser beam path. For each line-of-sight, the extracted data points include two freestream sections, two expanding flow sections, and the cylinder surface section, as seen in Fig. 7. The laser diameter shown in the schematic is not to scale. The locations of the line-of-sight extraction points depend on the size of the detector element, the distance the element is off the cylinder surface, and the angle of the element above the stagnation line. The plots in Fig. 8 show the shock-layer solutions of temperature, pressure, and mole fraction for both the noncatalytic and supercatalytic cases along the stagnation line. The most notable change between the two solutions is the mole fraction of CO_2 . For the supercatalytic case, the mole fraction at the surface returns to the freestream value. The mole fraction for the noncatalytic case is significantly lower. The pressure is relatively constant throughout the entire shock layer, as is the temperature until it drops down to the aluminum cylinder cold-wall temperature of 300 K; the test times in an expansion tunnel are short enough that the material does not have enough time to accommodate to the temperature of the gas behind the shock. The absorption line that is investigated is a low-temperature line; as temperature increases, the

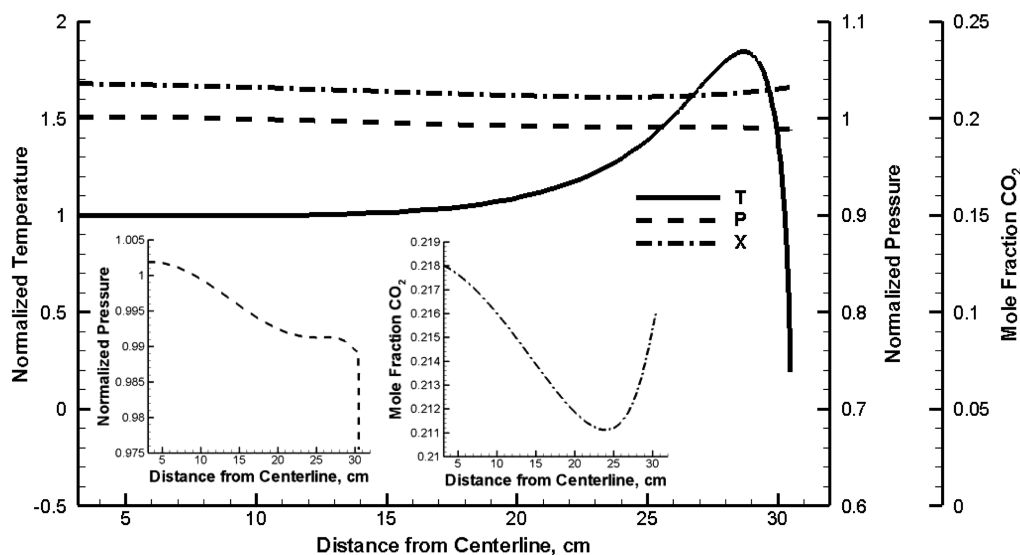


Fig. 6 Normalized temperature, normalized pressure, and mole fraction freestream profiles for tube half-width.

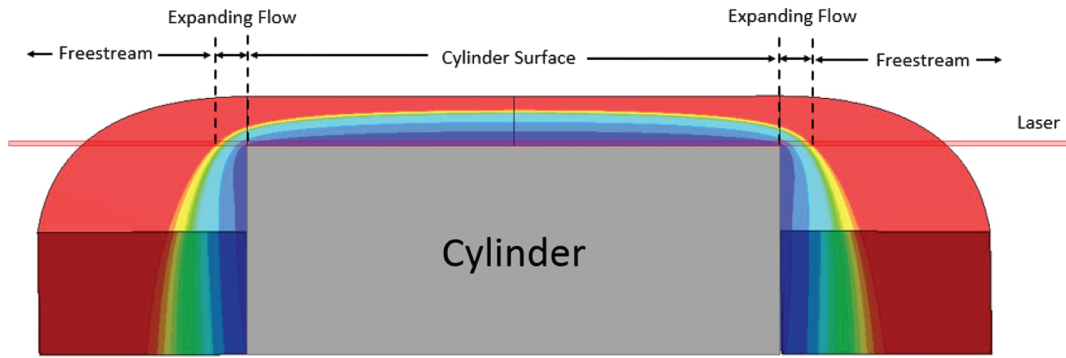


Fig. 7 Top view schematic of cylinder flow cut along stagnation line.

absorption decreases. The selected transition ensures that detection of CO_2 is more probable near the cylinder surface due to its sensitivity to low temperatures.

The LBL code uses the methodology in Sec. III.B to simulate each line-of-sight. The properties of the gas change throughout the line-of-sight, and it must therefore be split into homogeneous zones in order for the Beer–Lambert law to hold. This leads to the discretized form shown in Eqs. (6) and (7), in which the transmitted intensity from one homogeneous zone is used as the incident intensity for the next homogeneous zone. The individual lines-of-sight are averaged together at the end to simulate the entire detector element.

B. Sensitivity Studies

The experimental setup is constructed and documented as well as possible, but there is always a chance that some parameter varies slightly between the setup and the run. This section investigates the effects of slight perturbations from nominal conditions and their impact on the overall absorption spectrum. The base conditions used for each sensitivity study are a detector element width of $80 \mu\text{m}$ located at 5° above the stagnation line and $40 \mu\text{m}$ off the cylinder surface. Twenty polyline points normal to the cylinder surface are used for simulation in each case, except for the polyline point sensitivity case. The sensitivity studies investigate the following:

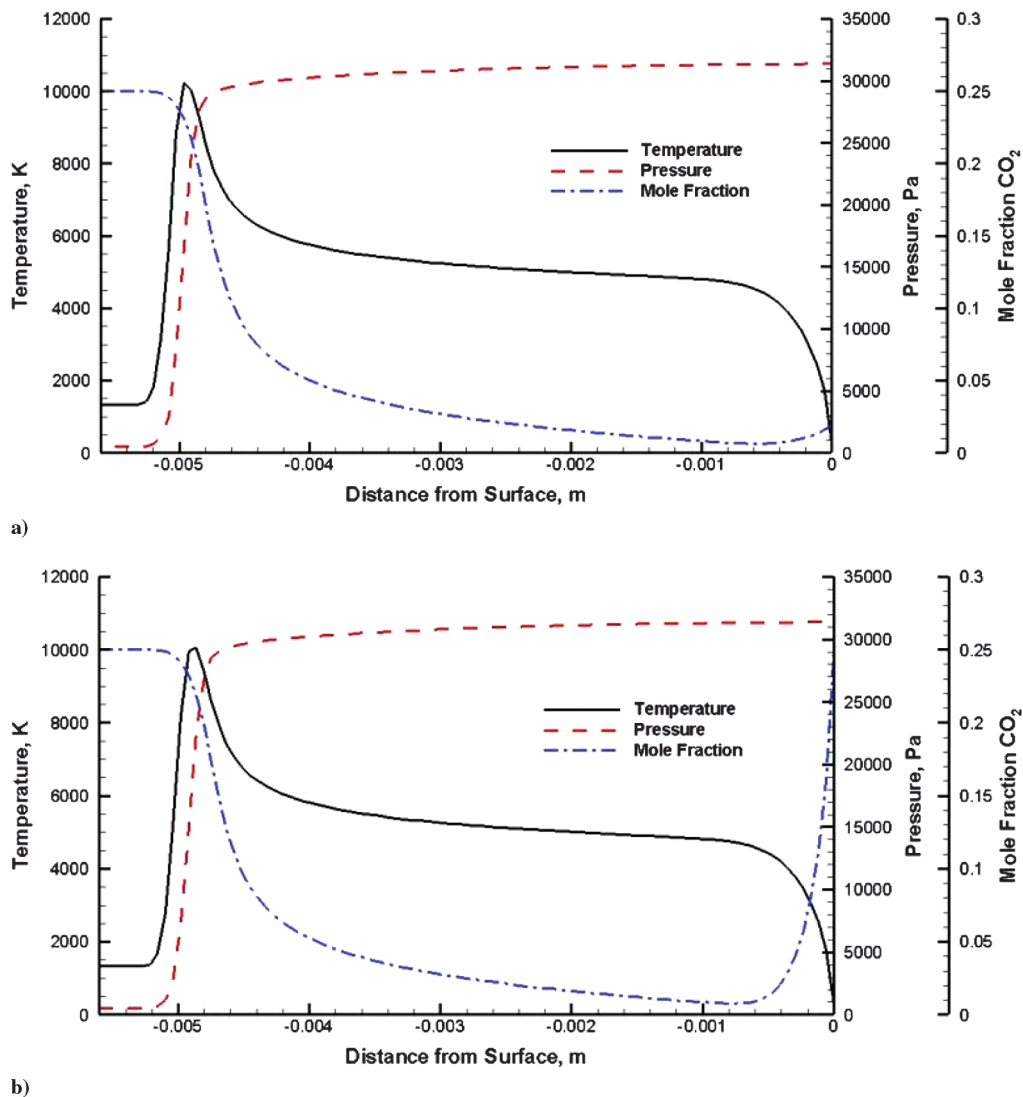


Fig. 8 Shock-layer profiles for temperature, pressure, and mole fraction for both the a) noncatalytic and b) supercatalytic cases.

detector element point independence, element size, element distance off the surface, element angle above the stagnation line, simulated element size, and expanding flow around the cylinder edge. A schematic illustrating these cases can be seen in Fig. 9.

The number of data points extracted from the CFD solution for use in the LBL simulation can range anywhere from a single point to hundreds of points. Plots of the transmission versus wavenumber are used to determine the minimum number of lines-of-sight that can be used in a simulation to obtain an accurate result. Lower numbers of points reduce computational time, but accuracy of the solution suffers. A plot of the spectra generated from the LBL code for varying numbers of lines-of-sight can be seen in Fig. 10. There is less than a 0.5% difference between using 20 points and 25 points, so 20 lines-of-sight are used for simulations for the remainder of the study.

The size of the detector element is determined before the run. With knowledge of the magnification of the optical system, the imaged size of each detector element is determined from the actual element dimension. A screw with known thread pitch is placed along the surface of the cylinder in the laser beam path and imaged onto an IR camera. A hollow tube is also placed along the cylinder surface approximately along the stagnation line. The hollow tube has an outer diameter of 1.4732 mm and an inner diameter of 1.1684 mm. The wall thickness in the image is nearly uniform, indicating good alignment along the entire cylinder surface. Using information from both the hollow tube and the screw, a calibration of the IR camera pixel element to physical distance is made. The magnification is then determined, and it is applied to the pixel element of the 32-element IR detector. The detector element width is 250 μm . Accounting for 3.125-times magnification, the apparent size of the element in the flow is 80 μm . Pixel sizes of 70, 80, 83, and 90 μm are compared to investigate the effects on the total transmission. The maximum percent difference between the spectra for the noncatalytic case is 0.15%, and for the supercatalytic case, it is 1.47%.

When using a multielement (linear array) detector, the detector elements extend out from the cylinder surface into the flow. It is possible that the near-surface element is displaced from the surface of the cylinder out into the shock layer some distance, on the order of tens of micrometers. The transmission plots for both noncatalytic and supercatalytic simulations can be seen in Fig. 11. The high-temperature P48f transition can be seen at approximately 3682.73 cm^{-1} in these simulations, but it is lost in the noise of the raw data due to its low absorption. The measurement is sensitive to distances off the cylinder surface: more so for the supercatalytic case because the gradient of CO_2 mole fraction is large compared to the noncatalytic case. The maximum percent difference between the

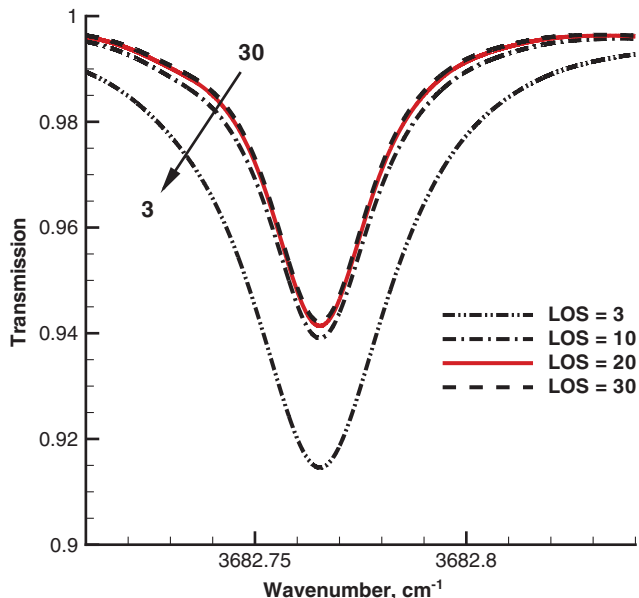


Fig. 10 Transmission plots for various number of polyline points extracted from the 2-D CFD results.

transmission plots for the noncatalytic and supercatalytic cases is 5.2 and 36.7%, respectively. Similarly, the maximum percent difference between the 0 μm case and the 40 μm case for $\gamma = 0.00025$ and $\gamma = 0.0005$ is 6.39 and 7.62%, respectively. It is imperative to accurately measure the distance of the detector element off the surface of the cylinder.

The effect of angular location above the stagnation line on the transmission spectrum is evaluated for angles of 0, 5, 10, 15, and 20 deg. An angle of 0 deg indicates an element on the stagnation line. As the angle increases, the transmission decreases (as more light is absorbed), though not significantly. The maximum percent difference between the spectra for the noncatalytic and supercatalytic cases is 0.15 and 1.58%, respectively.

When extracting data from the two-dimensional (2-D) CFD simulations, the height of the detector element has, up until now, been neglected because the property gradients are small along the vertical direction (radially around the cylinder). It was shown that 20 lines of sight along the horizontal direction of the detector element (perpendicular out from the cylinder surface) are sufficient to

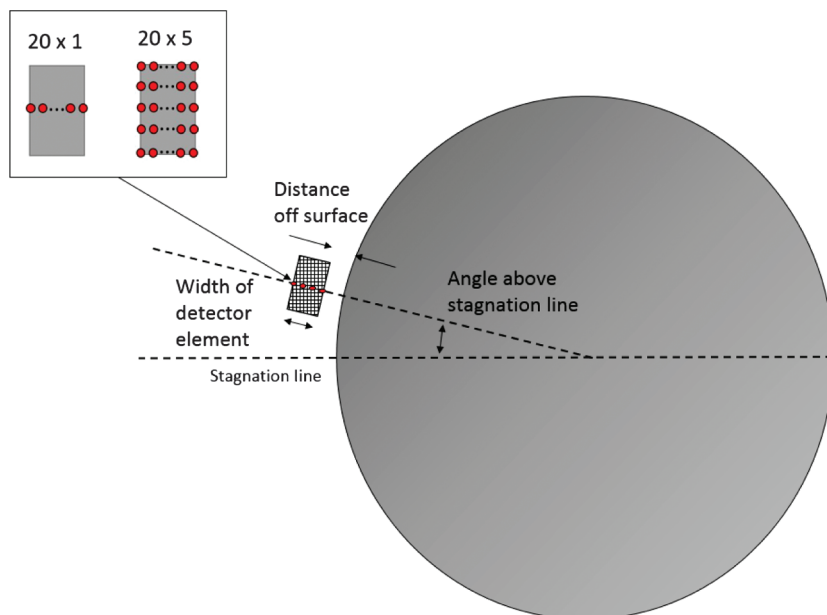


Fig. 9 Sensitivity studies schematic. Inset shows number of simulated points on detector element.

accurately simulate the flow. The first case is the 20×1 element simulation, in which 20 points are taken along the horizontal pixel direction (along the width). The second case is the 20×5 simulation, in which 20 points are taken along the horizontal direction at five vertical locations (along the height). The maximum percent difference between the transmission curves for noncatalytic and supercatalytic cases is 0.02 and 0.03%, respectively. The small differences indicate that the 20×1 method is sufficiently accurate for all simulations.

In three-dimensional flow around a cylinder, effects that are not seen in a simple two-dimensional simulation are introduced. One of these effects that has the potential to be important is the expanding flow around the edges of the cylinder. As the flow moves around the edges, the concentration changes along with pressure and temperature. The expansion section decreases the amount of freestream the laser travels through. However, it now needs to travel through this expansion region on both sides of the cylinder. Depending on the physical and chemical makeup of the gas, this region might increase the absorption through the path length. The path length the laser travels through the expanding flow on one side of the cylinder is 0.41 cm for the noncatalytic case and 0.49 cm for the supercatalytic case. Therefore, the total path lengths lost by the freestream to the expanding flow are 0.82 and 0.98 cm for the noncatalytic and supercatalytic cases, respectively. A schematic of the expanding flow can be seen in Fig. 7. The effect of including the expanding flow in the simulations on the transmission spectra is less than 0.1%, and it can be ignored.

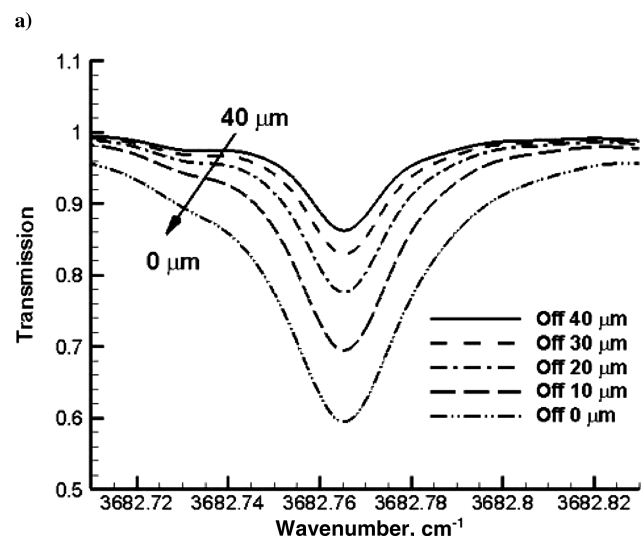
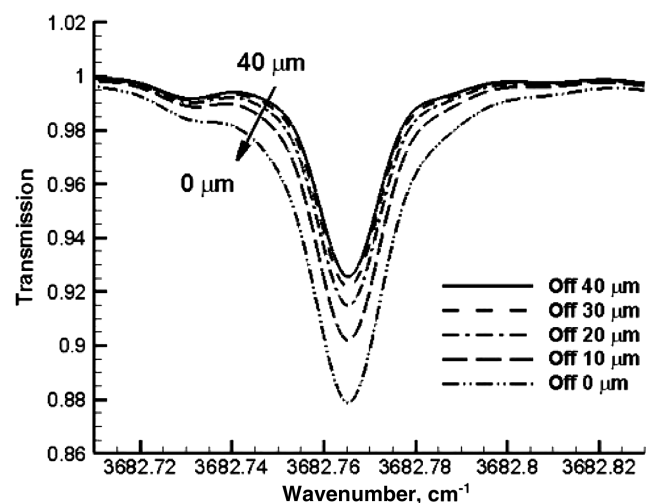


Fig. 11 Distance off cylinder surface comparisons for a) noncatalytic and b) supercatalytic cases.

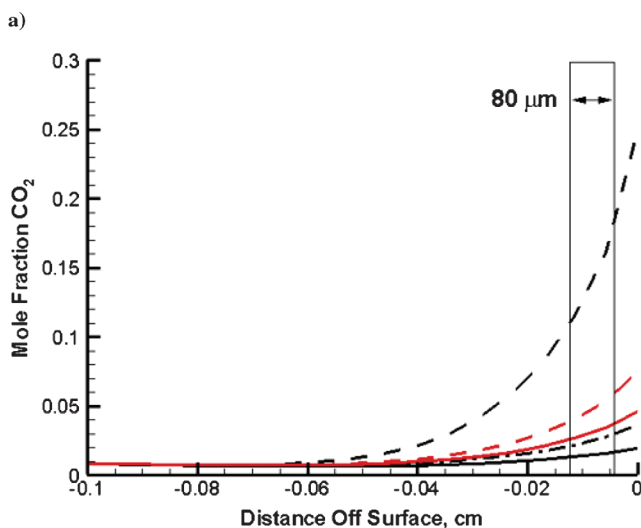
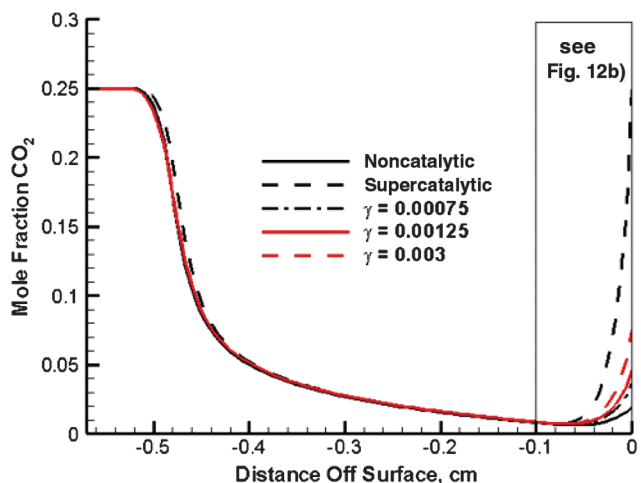


Fig. 12 Stagnation line mole fraction profiles in the shock layer for a) various reaction efficiencies, with b) zoom-in view of near-surface region.

C. Data and Simulation Comparison Results

With temperature and pressure profiles that are nearly the same in the shock layer for any recombination efficiency, the main sensitivity between absorption simulations is the concentration of CO_2 . A plot of

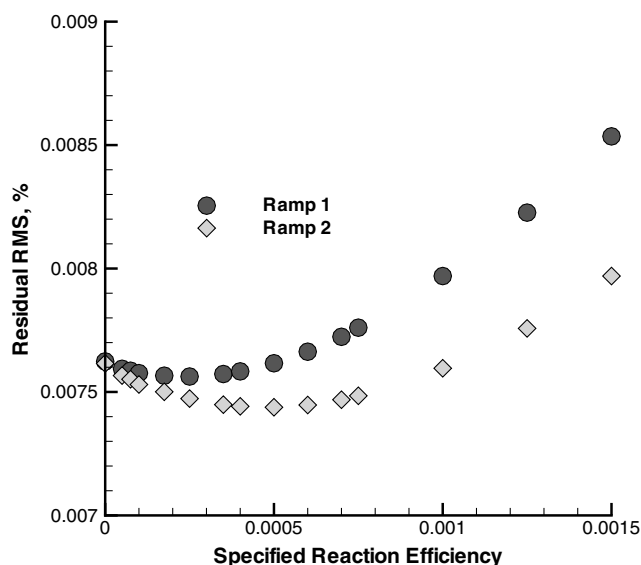


Fig. 13 RMS error of the residual between raw data and simulations for both ramp 1 and ramp 2.

the stagnation line profiles of the mole fraction of CO_2 in the shock layer for different reaction efficiencies can be seen in Fig. 12. There is a unique mole fraction profile for each reaction efficiency. Because of the particular absorption line selected, the maximum absorption sensitivity occurs immediately adjacent to the surface where the gas temperature is closest to the surface temperature of 300 K. If the exact size and position of the detector element in the flowfield is known, the simulations are able to determine which reaction efficiency produces CFD results that match the experimental data.

The LBL model simulates the cylinder region with a freestream region on each side of the cylinder. To compare the fit of the simulated results to the experimental data, the root mean square (RMS) of the residual between the calculation and the measured data points is computed. A plot of these values for each of the reaction efficiencies [0 (noncatalytic), 0.00005, 0.000075, 0.0001, 0.000175, 0.00025, 0.00035, 0.0004, 0.0005, 0.0006, 0.0007, 0.00075, 0.001, 0.00125, and 0.0015] is shown in Fig. 13. The minimum RMS gives the best fit of simulation to raw data. The consistency in the raw data from ramp 1 to ramp 2 indicates a steady measurement during the test time.

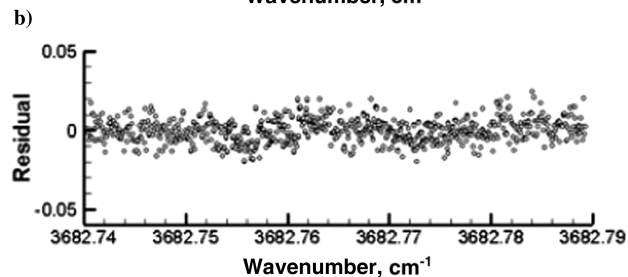
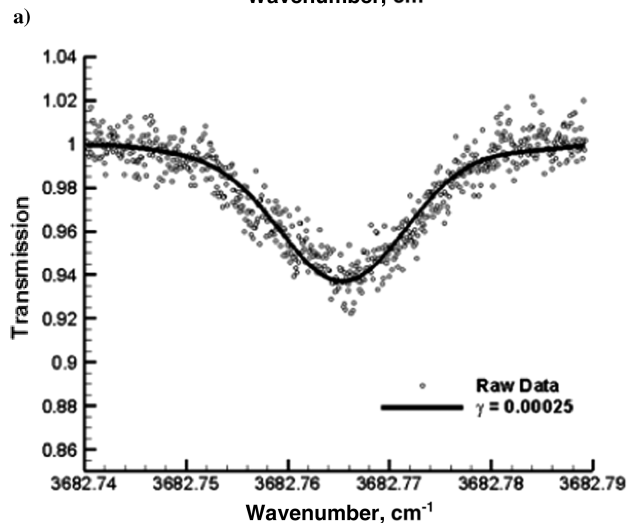
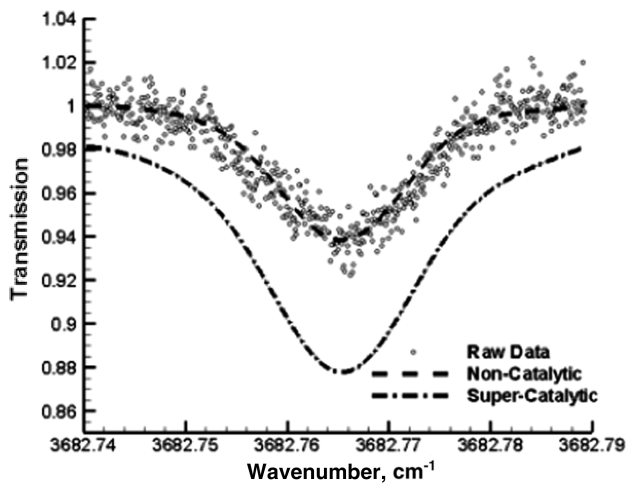


Fig. 14 Ramp 1 experimental results and simulations for noncatalytic, supercatalytic, and best fit.

Specified reaction efficiencies of 0.00025 and 0.0005 for ramp 1 and ramp 2, respectively, provide the best fit to the experimental data. Although this study focuses on an aluminum cylinder, these low recombination efficiencies are consistent with diffusion tube measurements on a variety of metal surfaces, indicating that surface reactions are not dominated by the reaction pathway leading to formation of CO_2 [44]. Preliminary measurements using an inductively coupled plasma facility also show minimal amounts of CO_2 near a highly catalytic water-cooled copper wall [45].

The plot in Fig. 14 shows the results for the noncatalytic, supercatalytic, and the best-fit reaction efficiency of 0.00025 for ramp 1, which is the first ramp after the arrival of the test gas. The plot in Fig. 15 shows the results for the noncatalytic, supercatalytic, and the best-fit reaction efficiency of 0.0005 for ramp 2, which was measured 250 μs later. These best-fit results agree with heat transfer distribution data observed indirectly in other experiments in LENS-XX, which has shown a low efficiency of surface catalysis in general,

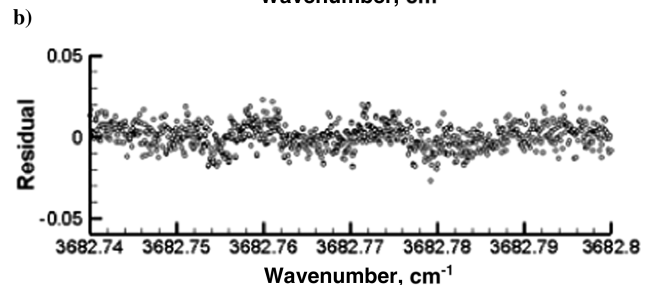
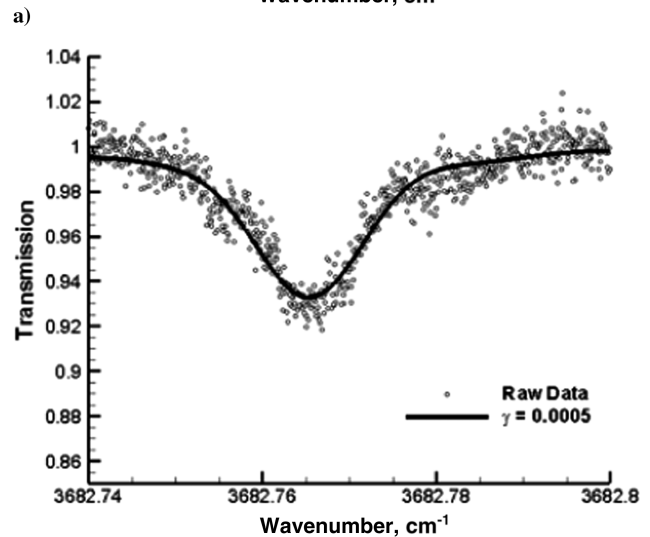
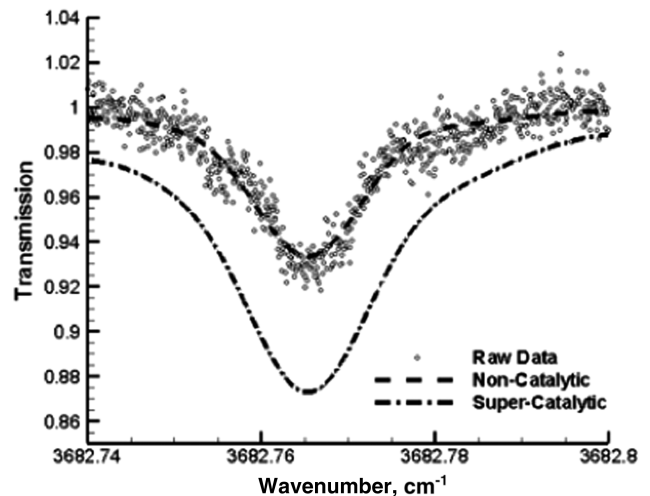


Fig. 15 Ramp 2 experimental results and simulations for noncatalytic, supercatalytic, and best fit.

and specifically for the CO + O mechanism [2,46]. This finding and others indicate that the design of TPS based on a supercatalytic boundary condition consistent with measurements made in previous ground test studies may have resulted in an overly conservative heat shield design.

V. Conclusions

An experimental setup using TDLAS was constructed to measure the concentration of CO₂ at the surface of a cylinder in order to describe the catalytic behavior of vehicles in hypersonic flows. Experimental data from the LENS-XX expansion tunnel were obtained for a 2-in.-diam 2.5-in.-long aluminum cylinder. The expansion tunnel has the benefit of an uncontaminated freestream gas composition, as opposed to reflected shock tunnels and arc jet facilities. The selected CO₂ P36e absorption line of the $\nu_1 + \nu_3$ rovibrational combination band is located at 3682.765 cm⁻¹, and it was chosen such that interference from other molecules over the laser beam path length was negligible. The DPLR and CHEETAh CFD codes were used to obtain numerical results for various catalytic reaction efficiencies for use in simulating the transmission spectrum. A line-by-line absorption code based off the discretized Beer-Lambert law was developed to use parameters obtained from the CFD simulations as inputs in order to simulate the transmission spectrum for comparison to experimental data. The raw data obtained in the experimental measurements were converted to transmission in wavenumber space for comparison to the simulations.

CFD solutions were obtained for cylinder flows in order to extract data along the cylinder surface and around the edges. The freestream flow profiles were obtained through a full facility DPLR simulation, coupled with results from CHEETAh. Sensitivity studies were carried out to investigate the effect of small perturbations in simulation parameters on the overall simulated transmission spectrum. Negligible perturbations include the detector element size, detector element angle above the stagnation line, expanding flow around the cylinder edges, and the number of lines used for the simulation of the pixel element. The detector element distance off the surface of the cylinder was important to know accurately. The actual simulation detector element size was 80 μm , located 40 μm off the cylinder surface, at an angle of 5 deg above the stagnation line. Simulations from various CFD solutions were plotted with the experimental data. The noncatalytic and supercatalytic solutions bound the data. Simulations were performed using different values of the catalytic recombination efficiency, and the best-fit value was $\gamma_{\text{CO}} = 0.00025$ to 0.0005 for both data ramps within the test time. This efficiency significantly limits the maximum energy reclamation possible at the surface, indicating that TPS designs can avoid using the conservative supercatalytic wall boundary condition for the design process. These results are an important step toward understanding the catalytic nature of vehicles in hypersonic flows, as well as in validating aerothermal CFD codes with ground test facilities.

A major goal of this effort was to design the experimental setup, validate the measurement technique, and develop the postprocessing and reconstruction process necessary to interpret the measured data. This objective has been successful, with the intent that this technique can also be used for the study of oxidizing carbon surfaces releasing carbon dioxide and carbon monoxide with the proper selection of higher-temperature absorption lines.

Acknowledgments

This work was sponsored by the U.S. Air Force Office of Scientific Research (AFOSR) under the Multidisciplinary University Research Initiative entitled Fundamental Processes in High-Temperature Hypersonic Flows, Prime Award FA9550-10-1-0563. The views and conclusions contained herein are those of the authors and should not be interpreted as necessarily representing the official policies or endorsements, either expressed or implied, of the AFOSR or the U.S. Government.

References

- [1] MacLean, M., and Holden, M., "Catalytic Effects on Heat Transfer Measurements for Aerothermal Studies with CO₂," *44th AIAA Aerospace Sciences Meeting and Exhibit*, AIAA Paper 2006-0182, 2006.
- [2] MacLean, M., Marineau, E., Parker, R., Dufrene, A., Holden, M., and DesJardin, P., "Effect of Surface Catalysis on Measured Heat Transfer in Expansion Tunnel Facility," *Journal of Spacecraft and Rockets*, Vol. 50, No. 2, 2012, pp. 470-475.
doi:10.2514/1.A32327
- [3] MacLean, M., Wadhams, T., Holden, M., and Hollis, B., "Investigation of Blunt Bodies with CO₂ Test Gas Including Catalytic Effects," *38th AIAA Thermophysics Conference*, AIAA Paper 2005-4693, 2005.
- [4] Marschall, J., and MacLean, M., "Finite-Rate Surface Chemistry Model, I: Formulation and Reaction System Examples," *42nd AIAA Thermophysics Conference*, AIAA Paper 2011-3783, 2011.
- [5] MacLean, M., Marschall, J., and Driver, D. M., "Finite-Rate Surface Chemistry Model, II: Coupling to Viscous Navier-Stokes Code," *42nd AIAA Thermophysics Conference*, AIAA Paper 2011-3784, 2011.
- [6] Zhou, X., Liu, X., Jeffries, J. B., and Hanson, R. K., "Development of a Sensor for Temperature and Water Concentration in Combustion Gases Using a Single Tunable Diode Laser," *Measurement Science Technology*, Vol. 14, No. 8, 2003, pp. 1459-1468.
doi:10.1088/0957-0233/14/8/335
- [7] Mohamed, A., Rosier, B., Henry, D., Louvet, Y., and Varghese, P. L., "Tunable Diode Laser Measurements on Nitric Oxide in a Hypersonic Wind Tunnel," *AIAA Journal*, Vol. 34, No. 3, 1996, pp. 494-499.
doi:10.2514/3.13095
- [8] Parker, R., Wakeman, T., MacLean, M., and Holden, M., "Measuring Nitric Oxide Freestream Concentration Using Quantum Cascade Lasers at CUBRC," *44th AIAA Aerospace Sciences Meeting and Exhibit*, AIAA Paper 2006-0926, 2006.
- [9] Pejakovic, D. A., Marschall, J., Duan, L., and Martin, M. P., "Nitric Oxide Production from Surface Recombination of Oxygen and Nitrogen Atoms," *Journal of Thermophysics and Heat Transfer*, Vol. 22, No. 2, 2008, pp. 178-186.
doi:10.2514/1.33073
- [10] Pejakovic, D. A., Marschall, J., Duan, L., and Martin, M. P., "Direct Detection of NO Produced by High-Temperature Surface-Catalyzed Atom Recombination," *Journal of Thermophysics and Heat Transfer*, Vol. 24, No. 3, 2010, pp. 603-611.
doi:10.2514/1.47175
- [11] Weisberger, J., DesJardin, P., MacLean, M., and R., Parker, "Near-Surface Nitric Oxide Concentration Measurement in the LENS-XX Expansion Tunnel Facility," *44th AIAA Thermophysics Conference*, AIAA Paper 2013-2643, 2013.
- [12] Gharavi, M., and Buckley, S. G., "Single Diode Laser Sensor for Wide-Range H₂O Temperature Measurements," *Applied Spectroscopy*, Vol. 58, No. 4, 2004, pp. 468-473.
doi:10.1366/000370204773580338
- [13] Barbu, T. L., Vinogradov, I., Durry, G., Korabev, O., Chassefière, E., and Bertaux, J. L., "TDLAS a Laser Diode Sensor for the In Situ Monitoring of H₂O, CO₂ and Their Isotopes in the Martian Atmosphere," *Advances in Space Research*, Vol. 38, No. 4, 2006, pp. 718-725.
doi:10.1016/j.asr.2005.04.049
- [14] Uddi, M., Das, A. K., and Sung, C., "Temperature Measurements in a Rapid Compression Machine Using Mid-Infrared H₂O Absorption Spectroscopy near 7.6 μm ," *Applied Optics*, Vol. 51, No. 22, 2012, pp. 5464-5476.
doi:10.1364/AO.51.005464
- [15] Vanderover, J., and Oehlschlaeger, M. A., "A Mid-Infrared Scanned-Wavelength Laser Absorption Sensor for Carbon Monoxide and Temperature Measurements from 900 to 4000 K," *Applied Physics B*, Vol. 99, Nos. 1-2, 2010, pp. 353-362.
doi:10.1007/s00340-009-3849-5
- [16] Farooq, A., Jeffries, J. B., and Hanson, R. K., "CO₂ Concentration and Temperature Sensor for Combustion Gases Using Diode-Laser Absorption near 2.7 μm ," *Applied Physics B*, Vol. 90, Nos. 3-4, 2008, pp. 619-628.
doi:10.1007/s00340-007-2925-y
- [17] Meyers, J. M., and Fletcher, D., "Diode Laser Absorption Sensor Design and Qualification for CO₂ Hypersonic Flows," *Journal of Thermophysics and Heat Transfer*, Vol. 25, No. 2, 2011, pp. 193-200.
doi:10.2514/1.49270
- [18] Pogány, A., Ott, O., Werhahn, O., and Ebert, V., "Towards Traceability in CO₂ Line Strength Measurements by TDLAS at 2.7 μm ," *Journal of Quantitative Spectroscopy and Radiative Transfer*, Vol. 130, Nov. 2013, pp. 147-157.
doi:10.1016/j.jqsrt.2013.07.011

- [19] Wu, K., Li, F., Cheng, X., Yang, Y., Lin, X., and Xia, Y., "Sensitive Detection of CO₂ Concentration and Temperature for hot Gases Using Quantum-Cascade Laser Absorption Spectroscopy near 4.2 μm," *Applied Physics B*, Vol. 117, No. 2, 2014, pp. 659–666. doi:10.1007/s00340-014-5880-4
- [20] Vallon, R., Soutadé, J., Vérant, J., Meyers, J., Paris, S., and Mohamed, A., "A Compact Tunable Diode Laser Absorption Spectrometer to Monitor CO₂ at 2.7 μm Wavelength in Hypersonic Flows," *Sensors*, Vol. 10, No. 6, 2010, pp. 6081–6091. doi:10.3390/s100606081
- [21] Dufrene, A., MacLean, M., Parker, R. A., Wadhams, T., and Holden, M., "Characterization of the New LENS Expansion Tunnel Facility," *48th AIAA Aerospace Sciences Meeting*, AIAA Paper 2010-1564, 2010.
- [22] Dufrene, A., MacLean, M., Parker, R., and Holden, M., "Experimental Characterization of the LENS Expansion Tunnel Facility Including Blunt Body Surface Heating," *49th AIAA Aerospace Sciences Meeting*, AIAA Paper 2011-0626, 2011.
- [23] Zhou, X., Jeffries, J. B., and Hanson, R. K., "Development of a Fast Temperature Sensor for Combustion Gases Using a Single Tunable Diode Laser," *Applied Physics B*, Vol. 81, No. 5, 2005, pp. 711–722. doi:10.1007/s00340-005-1934-y
- [24] Wright, M. J., Candler, G. V., and Bose, D., "Data-Parallel Line Relaxation Method for the Navier–Stokes Equations," *AIAA Journal*, Vol. 36, No. 9, 1998, pp. 1603–1609. doi:10.2514/2.586
- [25] MacCormack, R. W., and Candler, G. V., "The Solution of the Navier–Stokes Equations Using Gauss–Seidel Line Relaxation," *Computers and Fluids*, Vol. 17, No. 1, 1989, pp. 135–150. doi:10.1016/0045-7930(89)90012-1
- [26] Palmer, G. E., and Wright, M. J., "A Comparison of Methods to Compute High-Temperature Gas Viscosity," *8th AIAA/ASME Joint Thermophysics and Heat Transfer Conference*, AIAA Paper 2002-3342, 2002.
- [27] Palmer, G. E., and Wright, M. J., "A Comparison of Methods to Compute High-Temperature Gas Thermal Conductivity," *36th AIAA Thermophysics Conference*, AIAA Paper 2003-3342, 2003.
- [28] Gupta, R. N., Yos, J. M., Thompson, R. A., and Lee, K. P., "A Review of Reaction Rates and Thermodynamic and Transport Properties for an 11-Species Air Model for Chemical and Thermal Nonequilibrium Calculations to 30,000 K," NASA Rept. RP-1232, Aug. 1990.
- [29] Wright, M. J., Bose, D., Palmer, G. E., and Levin, E., "Recommended Collision Integrals for Transport Property Computations, Part 1: Air Species," *AIAA Journal*, Vol. 43, No. 12, 2005, pp. 2558–2564. doi:10.2514/1.16713
- [30] Wright, M. J., Hwang, H. H., and Schwenke, D. W., "Recommended Collision Integrals for Transport Property Computations, Part 2: Mars and Venus Entries," *AIAA Journal*, Vol. 45, No. 1, 2007, pp. 281–288. doi:10.2514/1.24523
- [31] Ramshaw, J. D., "Self-Consistent Effective Binary Diffusion in Multi-component Gas Mixtures," *Journal of Non-Equilibrium Thermodynamics*, Vol. 15, No. 3, 1990, pp. 295–300. doi:10.1515/jnet.1990.15.3.295
- [32] Park, C., Howe, J. T., Jaffe, R. L., and Candler, G. V., "Review of Chemical-Kinetic Problems of Future NASA Missions, II: Mars Entries," *Journal of Thermophysics and Heat Transfer*, Vol. 8, No. 1, 1994, pp. 9–23. doi:10.2514/3.496
- [33] Candler, G. V., "Chemistry of External Flows," *Aerothermochemistry for Hypersonic Technology*, von Kármán Inst. for Fluid Dynamics Lecture Series, VKILS 1995–04, von Karman Inst. for Fluid Dynamics, Rhode Saint Genèse, Belgium, April 1995, <http://www.worldcat.org/title/aerothermochemistry-for-hypersonic-technology-april-24-28-1995/oclc/33063455>.
- [34] Landau, L., and Teller, E., "Theory of Sound Dispersion," *Physikalische Zeitschrift der Sowjetunion*, Vol. 10, No. 1, 1936, pp. 34–43.
- [35] Millikan, R. C., and White, D. R., "Systematics of Vibrational Relaxation," *Journal of Chemical Physics*, Vol. 39, No. 12, 1963, pp. 3209–3213. doi:10.1063/1.1734182
- [36] Camac, M., "CO₂ Relaxation Processes in Shock Waves," *Fundamental Phenomena in Hypersonic Flow*, edited by Hall, J. G., Cornell Univ. Press, Ithaca, NY, 1964, pp. 195–215.
- [37] Park, C., "Assessment of Two-temperature Kinetic Model for Ionizing Air," *Journal of Thermophysics and Heat Transfer*, Vol. 3, No. 3, 1989, pp. 233–244. doi:10.2514/3.28771
- [38] Bose, D., Wright, M. J., and Palmer, G. E., "Uncertainty Analysis of Laminar Aeroheating Predictions for Mars Entries," *Journal of Thermophysics and Heat Transfer*, Vol. 20, No. 4, 2006, pp. 652–662. doi:10.2514/1.20993
- [39] Sepka, S., Chen, Y. K., Marschall, J., and Copeland, R. A., "Experimental Investigation of Surface Reactions in Carbon Monoxide and Oxygen Mixtures," *Journal of Thermophysics and Heat Transfer*, Vol. 14, No. 1, 2000, pp. 45–52. doi:10.2514/2.6488
- [40] Davis, M. E., and Davis, R. J., *Fundamentals of Chemical Reaction Engineering*, McGraw-Hill, Boston, 2003, pp. 133–134.
- [41] Wright, M. J., Olejniczak, J., Brown, J. L., Hornung, H. G., and Edquist, K. T., "Modeling of Shock Tunnel Aeroheating Data on the Mars Science Laboratory Aeroshell," *Journal of Thermophysics and Heat Transfer*, Vol. 20, No. 4, 2006, pp. 641–651. doi:10.2514/1.19896
- [42] Rothman, L. S., et al., "The HITRAN 2008 Molecular Spectroscopic Database," *Journal of Quantitative Spectroscopy and Radiative Transfer*, Vol. 110, Nos. 9–10, pp. 533–572, 2009. doi:10.1016/j.jqsrt.2009.02.013
- [43] McLean, A. B., Mitchell, C. E. J., and Swanston, D. M., "Implementation of an Efficient Analytical Approximation to the Voigt Function for Photoemission Lineshape Analysis," *Journal of Electron Spectroscopy and Related Phenomena*, Vol. 69, No. 2, 1994, pp. 125–132. doi:10.1016/0368-2048(94)02189-7
- [44] Marschall, J., Copeland, R. A., Hwang, H. H., and Wright, M. J., "Surface Catalysis Experiments on Metal Surfaces in Oxygen and Carbon Monoxide Mixtures," *44th AIAA Aerospace Sciences Meeting and Exhibit*, AIAA Paper 2006-0181, 2006.
- [45] Meyers, J. M., Owens, W. P., Uhl, J., and Fletcher, D. G., "Near Surface CO₂ Detection in an Inductively Couple Plasma Facility Using Diode Laser Absorption," *42nd AIAA Thermophysics Conference*, AIAA Paper 2011-3788, 2011.
- [46] MacLean, M., Dufrene, A., and Holden, M., "Spherical Capsule Heating in High Enthalpy Carbon Dioxide in LENS-XX Expansion Tunnel," *51st AIAA Aerospace Sciences Meeting Including the New Horizons Forum and Aerospace Exposition*, AIAA Paper 2013-0906, 2013.

G. Palmer
Associate Editor